Geophysical Characterization of the Salna Sinking Zone, Garhwal Himalaya, India

Rambhatla G. Sastry · Suman K. Mondal

Abstract Infrastructure and communication facilities are repeatedly affected by ground deformation in Gharwal Himalaya, India; for effective remediation measures, a thorough understanding of the real reasons for these movements is needed. In this regard, we undertook an integrated geophysical and geotechnical study of the Salna sinking zone close to the Main Central Thrust in Garhwal Himalaya. Our geophysical data include eight combined electrical resistivity tomography (ERT) and induced polarization imaging (IPI) profiles spanning 144–600 m, with 3–10 m electrode separation in the Wenner–Schlumberger configuration, and five micro-gravity profiles with 10–30 m station spacing covering the study region. The ERT sections clearly outline the heterogeneity in the subsurface lithology. Further, the ERT, IPI, and shaliness (shaleyness) sections infer the absence of clayey horizons and slip surfaces at depth. However, the Bouguer gravity analysis has revealed the existence of several faults in the subsurface, much beyond the reach of the majority of ERT sections. These inferred vertical to subvertical faults run parallel to the existing major lineaments and tectonic elements of the study region. The crisscross network of inferred faults has divided the entire study region into several blocks in the subsurface. Our studies stress that the sinking of the Salna village area is presently taking place along these inferred vertical to subvertical faults. The Chamoli earthquake in March 1999 probably triggered seismically induced ground movements in this region. The absence of few gravity-inferred faults in shallow ERT sections may hint at blind faults, which could serve as future source(s) for geohazards in the study region. Soil samples at two sites of study region were studied in a geotechnical laboratory. These, along with stability studies along four slope sections, have indicated the critical state of the study region. Thus, our integrated studies emphasize the crucial role of micro-gravity in finding fine subsurface structure at deeper depth level; supported by ERT and IPI at shallow depth

R. G. Sastry (✉)
Department of Earth Sciences, IIT Roorkee, Roorkee, Uttarakhand State 247667, India
e-mail: rgssastry@gmail.com; rgss1fes@iitr.ernet.in

S. K. Mondal
Capstone Geo Consultants (India) Pvt. Ltd., #404, 4th Floor, Sri Nivas Homes,
Above Axis Bank, Peerzadiguda, Uppal, Hyderabad 500 092, India
e-mail: suman@cgcl.in; suman.k.mondal@gmail.com

intervals, they can satisfactorily explain the Salna sinking zone close to Lesser Himalaya. The geotechnical studies also lend support to these findings. These integrated studies have yielded a better understanding of the mass-wasting mechanism for the study region.

Keywords Geohazards · Sinking zone · Landslides · Gravity survey · Electrical resistivity tomography · Induced polarization tomography · Slope stability study

1 Introduction

Mass movements are geohazards that can directly influence human existence in mountainous terrains. The Indian Himalayan belt, which supports a wide variety of ecosystems, is prone to various types of natural disasters due to its geological conditions and typical climatic conditions. Landslides occur both in the Lesser and in the Higher Himalayas and also in the barren cold desert regions of Ladakh.

In areas prone to landslides, communication infrastructure often has to be repaired. Many repairs are made without getting any substantial benefit because of the lack of a full understanding of the geometry and hydrologic regime of the affected sites and the landslide processes (Bogoslovsky and Ogilvy 1977). In addition, the blind implementation of a traditional engineering repair schemes, for example recompaction, may not serve to mitigate adequately all types of future slope stability (McCann and Forster 1990). Scores of different methods (Pachauri and Pant 1992; Rautela and Lakhera 2000; Sarkar and Kanungo 2002; Saha et al. 2005) for assessing landslide hazards have been proposed. However, a common ground is lacking in the preparation of landslide hazard zonation (LHZ) maps by different specialists such as geo-environmentalists, engineers, policy-makers, or developers in hilly regions. Besides, these zonation maps in general do not consider the subsurface conditions or parameters, which play a major role in landslide processes.

Geophysical methods are non-invasive and in situ, and the results of many of them can be translated into relevant geotechnical information on the subsoil (Cosenza et al. 2006). Geophysical methods can provide highly resolved two-dimensional distributed data (Mauritsch et al. 2000). A particular geophysical method may not be suitable to study all types of mass movement processes. A careful selection of one method or a combination of several methods is necessary, by considering the local geological and structural setting and the type of mass movement. By applying appropriate geophysical interpretation, three-dimensional models of the investigated slope may be developed (McCann and Forster 1990; Mauritsch et al. 2000, Lebourg et al. 2003). Also, geophysical methods provide new means for the rapid investigation of vast areas at a relatively low cost (Bogoslovsky and Ogilvy 1977).

Electrical resistivity is sensitive to four parameters, viz., the water content, the mineralization of pore water, the cation exchange capacity of clay minerals, and temperature (Revil et al. 1998, 2002; Niwas et al. 2007; Jin et al. 2007; Shevnin et al. 2007; Hayley et al. 2007). Some of these parameters can play an important role in landslide processes, so this is the reason why ERT finds a natural application in landslide investigations. The role of micro-gravity in near-surface investigations is well recognized in the geophysical literature (Loj 2010; Rybakov et al. 2001).

Lebourg et al. (2003) studied deep-seated landslides in the French Alps through 2D and 3D geophysical imaging methods. Scores of authors (Erginal et al. 2009; Piegari et al. 2009; Havenith et al. 2000; Bichler et al. 2004; Lapenna et al. 2003, 2005; Colangelo et al. 2006; Friedel et al. 2006; Jomard et al. 2007; Sastry et al. 2006, 2007, 2008; Mondal et al.

2007, 2008; Park 1998) have utilized and discussed various geophysical methods in order to delineate the plane of failure, the hydrogeological regime, and to monitor the activity of the landslide. 3D and 4D ERT (Chambers et al. 2011; Wilkinson et al. 2010; Jongmans and Garambois 2007; Schmutz et al. 2009; Friedel et al. 2006; Lebourg et al. 2005) and fast 2D (Bichler et al. 2004; Perrone et al. 2004; Yang et al. 2004; Lapenna et al. 2003, 2005; Lebourg et al. 2005; Drahor et al. 2006; Sastry et al. 2006, 2007, 2008; Mondal et al. 2007) have also been used for landslide studies. The utility of ERT to investigate roto-translational slides and a translational earth flow in southern Italy are discussed by Lapenna et al. (2005). Israil and Pachauri (2003) have utilized a joint application of vertical electrical sounding (VES), seismic refraction, and the spectral analysis of surface waves (SASW) to characterize a landslide in Himalayan foothills region. Active landslide characterization using the 2D ERT method (Sastry et al. 2006; Mondal et al. 2007, 2008) and a combined application of 2D ERT and the gravity method have been discussed by Sastry et al. (2007, 2008).

Gravity surveys could reveal the subsurface slope morphology (Sastry et al. 2008), while lithological variations leading to bulk density variations are used for quantitative slope stability analysis (Del Gaudio et al. 2000). Del Gaudio et al. (2000) have also discussed the use of a micro-gravity survey on slump earth flows in Italy. Bláha et al. (1998) claimed that gravimetric surveys provided an effective contribution to the description of the structures and their dynamic control over time. Gravity measurements can detect local faults and subsurface failure surfaces both within the slide mass and in its vicinity, and they can contribute to a better characterization of active landslides (Sastry et al. 2007).

As per Jongmans and Garambois (2007), induced polarization methods have not been applied so far to landslide problems even though IP method can distinguish clayey zones from water-saturated zones, which exhibit almost the same resistivities. Recently, Zanetell (2011) has used both IP and seismic methods for landslide investigations. Here, we employ ERT, IPI, and gravity method in addressing the active landslide at the Salna sinking zone. The geophysical investigations included gravity, ERT, and IPI methods. Gravity has helped decipher several faults, which seem to control the sinking zone. ERT and IPI profiles infer the shallow geological structures and lithologies with fault signatures. Geotechnical soil classification has been carried out at two test sites, and slope stability studies were carried out along four slope profiles. These integrated studies have led a new understanding of the reasons for the sinking region at Salna, India.

2 Study Area and Physiography

The Himalayan mountain chains are seismically very active. Many small earthquakes occur almost every day along some of the neo-tectonically active fault zones (Rao et al. 2006; Bilham et al. 2001; Gaur et al. 1984; Kayal 2001; Khattri and Tyagi 1983; Khattri et al. 1989; Ni and Barazangi 1984; Sarkar et al. 1993). The tectonic activities due to earthquakes along numerous faults in the Himalaya have resulted in contemporary morphological adjustments, inducing a variety of mass-wasting processes (Saraf 2000). The Chamoli earthquake not only triggered many new landslides, but also reactivated old ones (Ravindran and Philip 1999). One reactivated mass movement site is the sinking zone developed near the village of Salna in the Chamoli district of Uttarakhand. A portion of almost 200 m of the Pokhri–Gopeshwar motor road has sunk 20 m vertically (Fig. 1a) since 1999 and a landslide buried several residential buildings and acres of cultivated land (Fig. 1b).

Fig. 1 **a** Sinking of the Pokhri—Gopeshwar road. The *arrow* compensates the earlier elevation of the road to the present one. **b** A scenic view of the Salna village sinking zone showing the destruction of cultivated land due to sinking
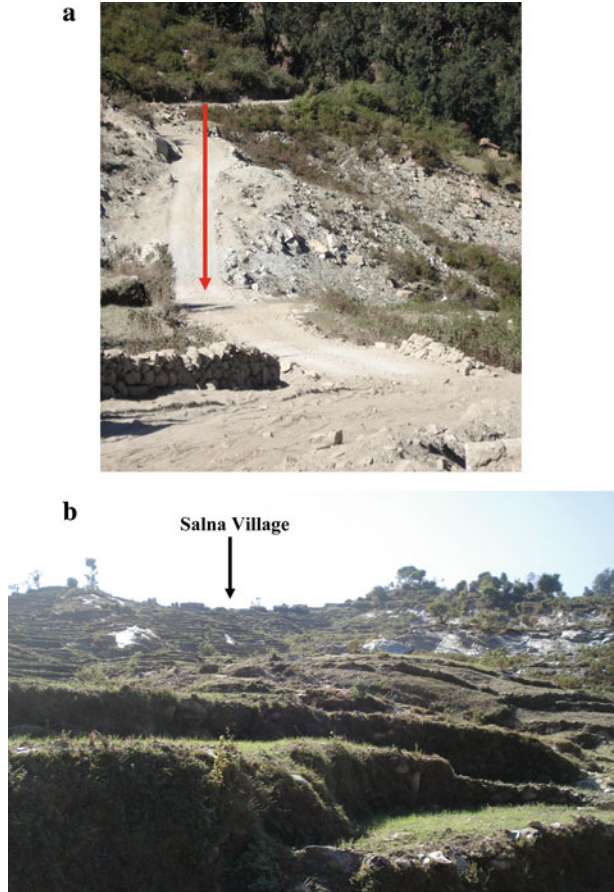
Salna village is a small hamlet of about 200 people in Pokhri tehsil of the Chamoli district of Uttarakhand, India. The Salna village sinking zone (30°23′44″N, 79°12′13″E) is located at the right side of Nagol gad (river) immediately to the northeast corner of the village Salna, at 11 km from Pokhri along Pokhri—Gopeshwar road (Fig. 2), a distance of about 220 km from the state capital Dehradun. This road serves as an alternate for National Highway No. 58 and connects two major tourist attraction sites, Badrinath and Kedarnath. Further, this road is the only means of communication for the inhabitants of the northwest Alkananda valley to access major towns like Gopeshwar (at 55 km) in the North, Rudraprayag (70 km) in the West, and Karnaprayag (40 km) to the South of the landslide site.

A major part of this landslide slope is covered with cultivated land as terrace farming. The slope has a gradient of 50–60° in the vicinity of the landslide. The elevation difference between the toe (1,380 m above msl) and the crown (1,500 m above msl) of the landslide is around 120 m. The annual temperature varies from 5 °C in January to 35 °C in June or July. Nearly 70 % of the rainfall occurs during the period of June to September and the average annual rainfall varies from 1,200 to 1,500 mm. The relative humidity in
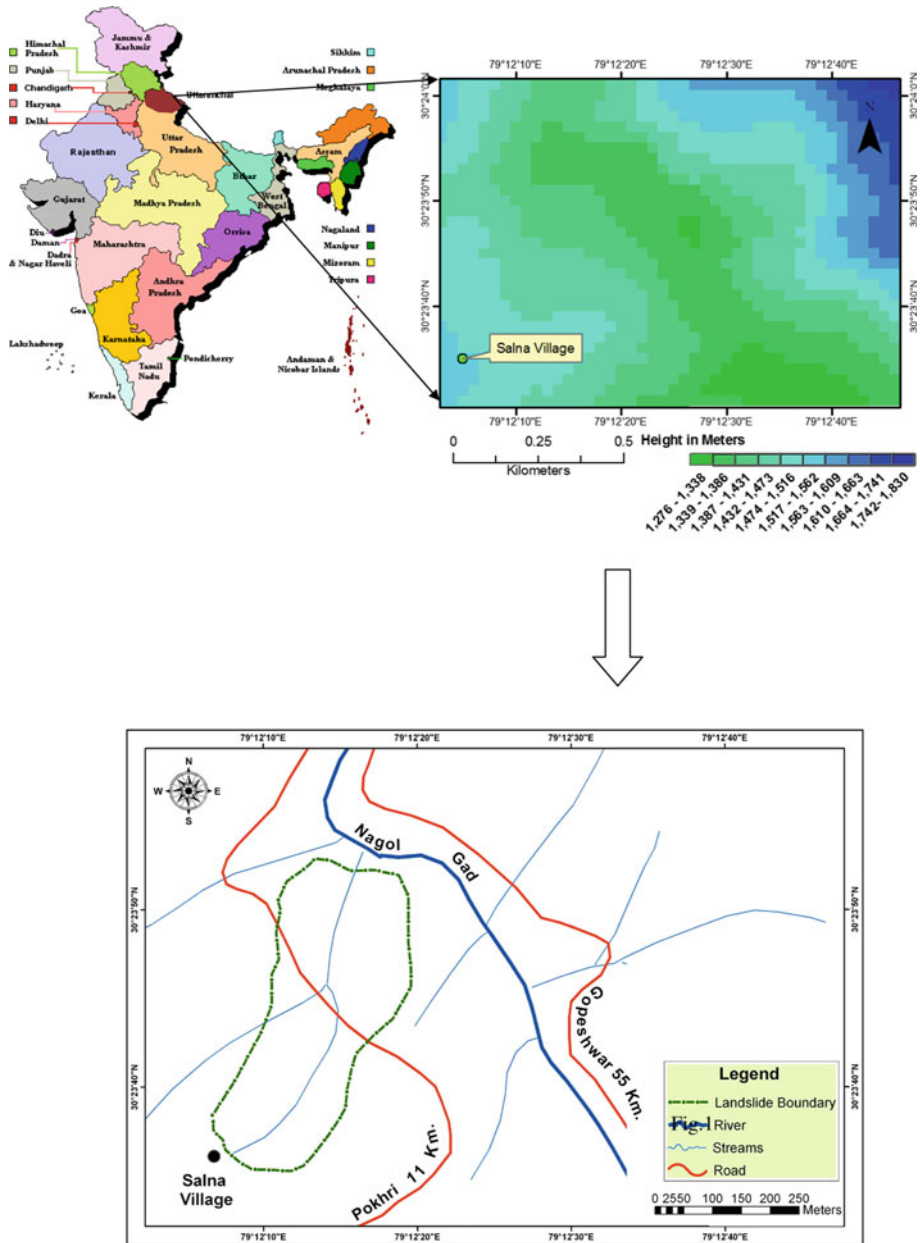
Fig. 2 Map showing the location of the Salna village sinking zone, Uttarakhand, India. The Digital Elevation Model (DEM) of the study region is prepared using ASTER GDEM (ArcGIS 9.3), which has a ground resolution of 30 m. In the image, the height values are grouped according to their increasing values (Aster GDEM is freely downloadable from http://www.gdem.aster.ersdac.or.jp)

the area is high during the monsoon season, generally exceeding 70 % on the average. The driest part of the year is the pre-monsoon period when the humidity drops to 35 % in the afternoon.

3 Geological Setting

The study area (Fig. 2) was marked by a complex geological setting (Fig. 3) with a large number of litho-units, which comprise of quartzite, phyllite, schists, gneisses, and meta-volcanics of various genres (Kumar and Agarwal 1975). Regionally, the geological setup comprises the Garhwal group of rocks, which were sandwiched between the northern bound of Central Crystallines and the southern bound of Dudatoli group. Both boundaries were of tectonic origin and were thrust faults. The Main Central Thrust (MCT) marks the boundary between the Central Crystallines (Fig. 3) and the Garhwal group of rocks, while the North Almora Thrust (not shown on the present map) marks the boundary between the Garhwal group and the Dudatoli group. The present study site was a part of the Patroli formation of the Garhwal group (Kumar and Agarwal 1975), which was bounded by these two major regional thrust faults. This group was broadly divided into five formations, namely Rudraprayag, Lameri, Chamoli, Gwanagarh, and Patroli.

The Garhwal group consists of quartzite, phyllite, slate, and limestone. Acidic and basic igneous rocks intruded the Garhwal group. The structures of the Garhwal group of rocks around the study area were complicated due to the effects of various tectonic episodes. There were at least three phases of tectonic activity, which are clearly visible in the present day regional structural patterns (Kumar and Agarwal 1975). The second generation NE-SW trending broad and open plunging folds and faults were superimposed on the earlier NW-SE doubly plunging folds and faults, such as the Maithana syncline. Toward the end of this period, a large number of NW-SE trending faults, such as the Kande and
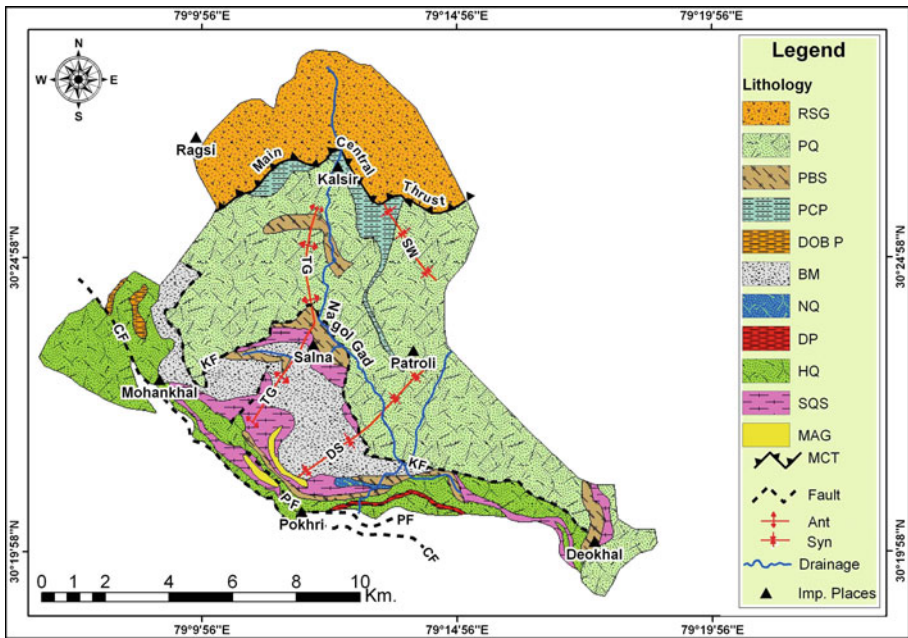

Fig. 3 Geological map of the study area (after Kumar and Agarwal 1975). *Notation RSG* Ragsi Schist and Granite, *PQ* Patroli Quartzites, *PBS* Patroli Biotite Schist, *PCP* Patroli Chlorite Phylite, *DOB P* Dobri Phylite, *BM* Bhekuna Metavolcanics, *NQ* Nagthat Quartzite, *DP* Deothan Phylite, *HQ* Hariali Quartzite, *SQS* Sericite Quartz Schist, *MAG* Magnesite, *CF* Chamethi Fault, *PF* Pokhri Fault, *KF* Kande Fault, *TG* Tangi Anticline, *MS* Maithana Syncline, *DS* Dudhbhanga Syncline, and *Ant/Syn* Anticline/Syncline Axis

Chamethi faults were developed resulting in the mylonitisation of granite giving rise to sericite quartz schist. Due to the Main Central Thrust, the closer part of the southeasterly plunging Maithana syncline was terminated near Kalsir. The Chamethi and Pokhri faults are two parallel faults, which die out eastward and continue westward beyond Mohankhal. The other two major structures are the Tangi anticline and the Dudhbhanga syncline (Kumar and Agarwal 1975). The rocks exposed in the vicinity of the landslide site are biotite schist and sericite quartz schist of the Patroli formation of the Garhwal group. The landslide is located less than 300 m from the Kande Fault in the North–East and the Tangi Anticline in the North–West directions.

4 Geophysical Investigations

A SYSCAL Jr *Switch—72* DC electrical resistivity imaging system of IRIS Instruments was used for ERT and IPI studies. This is a multi-node resistivity imaging system (www.iris-instruments.com) with an internal switching board for 72 electrodes and an internal 100 W power source. For sequence preparation, Electre II was used. The locations of the geophysical profiles are shown in Fig. 4. A total of eight combined ERT and IPI profiles along profiles AA′, BB′, CC′, DD′, EE′, FF′, GG′ & HH′ (Fig. 4) were undertaken during June 2006 using a Wenner–Schlumberger array configuration with different inter-electrode spacings. Relevant data acquisition details are included in Table 1.

The CG-5 Micro-gravimeter (M/S Scintrex make) has been employed for gravity data acquisition (Fig. 4) with a station interval of 10–30 m at 68 stations, in five different profiles (Gravity profiles 1, 2, 3, 4, and 5). Gravity profile 1 was conducted along the road,
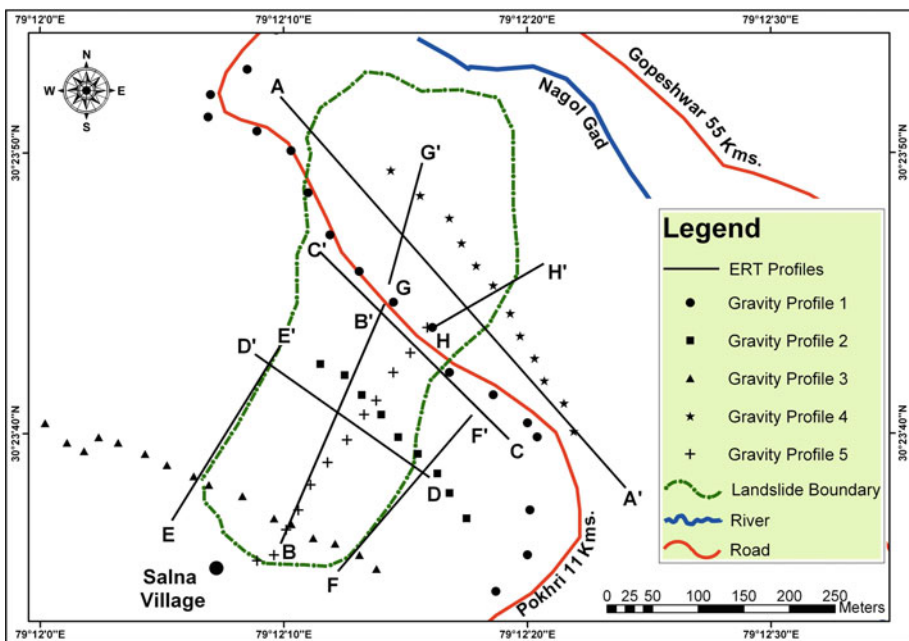
Fig. 4 Map showing the location of the ERT (AA′ to HH′), IP (AA′ to HH′) and gravity profiles (Profiles 1, 2, 3, 4 and 5). The landslide boundary is marked by the *green dashed line*

Table 1 ERT and IPI data acquisition details

Sl. no.	Profile	ERT & IPI (Fig. 4)			
		Electrode separation (m)	No. of electrodes	Profile length (m)	Investigation depth (m)
1	AA′	10	60	600	90
2	BB′	5	60	300	45
3	CC′	5	60	300	45
4	DD′	5	48	240	45
5	EE′	5	48	240	40
6	FF′	5	48	240	45
7	GG′	3	48	144	27
8	HH′	3	48	144	27

profiles 2, 3, and 4 were carried out in parallel to profile 1 in the central part of landslide, at the crown and near the toe regions, respectively. Profile 5 was conducted parallel to the landslide axis. The positioning of the electrodes of multi-electrode resistivity system and the gravity stations was completed with a Leica CS 5 GPS and a Topcon GTS 710 electronic total station.

For assessing the average density of hard rock, both laboratory density measurements of collected hard rock samples from landslide and adjacent areas and in situ overburden density estimation using a core cutter (Ranjan and Rao 2005) were carried out.

4.1 Geophysical Data Processing and Interpretation

The geophysical data sets include ERT, IPI, and micro-gravity. Interpretation of geophysical data is made through knowledge gained from extensive fieldwork done at the site and through the available literature. The processing and interpretation details are mentioned below.

4.1.1 ERT & IPI Data Processing and Interpretation

Both ERT and IPI data were processed using IRIS software and inverted respectively to 2-D true resistivity (RES2DINV software of Loke 2006) and chargeability sections using the Loke and Barker (1995a, b, 1996a, b) and Oldenburg and Li (1994) algorithms. Based on outcrops and the geoelectrical literature (Telford et al. 1990), resistivity–lithology and chargeability–lithology conversions (Tables 3, 4) were prepared, which served as the basis for the preparation of litho-sections along profiles AA′, BB′, CC′, DD′, EE′, FF′, GG′ & HH′ (Fig. 4), and also for their common color code presentation. The IPI sections were performed along with the ERT data along profiles AA′, BB′, CC′, DD′, EE′, FF′, GG′ & HH′ (Fig. 4). A common color code is developed and adopted for the presentation of true chargeability sections along all the profiles. The true chargeability variation ranged from 0.01 to 153 mV/V.

4.1.2 Shaliness Estimation

Here, we estimated the relative shaliness (shaleyness) of the subsurface materials from true chargeability data using the following formula similar to the one proposed in the well-logging literature (Serra 1984).

$$SHP = \frac{CHT - CHT_{Min}}{CHT_{Max} - CHT_{Min}}\% \qquad (1)$$

where SHP is the relative shaliness percentage, CHT the present true chargeability within the subsurface, CHT_{Min} the minimum true chargeability, and CHT_{Max} the maximum true chargeability.

Table 2 was adopted for the assigning the shaliness to the lithologies. The IPI (True Chargeability) section can be converted to a relative shaliness plot, which in turn can infer broad lithologies. Relative shaliness may not literally mean the presence of clay/shale. However, such plots can serve as additional constraints to ERT plots for lithological information on the subsurface. Also, these plots need to be analyzed with respect to the local geology of a site.

4.1.3 Gravity Data Processing and Interpretation

Interpretation of ERT and IPI sections was first needed to be able to process the gravity data. By considering the resistivity images, a Bouguer datum was selected which led to the Bouguer anomaly map of the study region. The Bouguer gravity anomaly map was subjected to both qualitative and quantitative interpretation. The qualitative interpretation involved identification of fault signatures and their role on the structurally controlled landslides. Then, several gravity profiles were drawn on the Bouguer anomaly map across the strike of inferred faults, and they were subjected to quantitative interpretation for fault parameters.

4.1.4 Density Contrast Estimation

Laboratory density measurements of collected hard rock samples from landslide and adjacent areas were carried out to assess the average density of hard rock. The in situ overburden density was measured using a core cutter (Ranjan and Rao 2005). The lateral density contrast was estimated using the above density values.

5 Results and Discussion

As per the procedure outline earlier, ERT, IPI, and gravity data analysis results are considered here with relevant discussions in the relevant subsections. Some illustrative examples are considered.

5.1 Development of Resistivity–Lithology and Chargeability–Lithology Conversion Tables

As mentioned earlier, based on the outcrops and geoelectrical literature (Telford et al. 1990), resistivity–lithology and chargeability–lithology conversion tables (Tables 3, 4)

Table 2 Percentage of shaliness and related lithology	Shaliness %	Formation
	0–20	Sand
	20–50	Sandy clay
	50–70	Clayey sand
	70–100	Clay

were prepared. From the current experience of geophysicists the world over, by no means can one claim uniqueness in developing such conversion tables. However, special care was taken in designing these conversion tables placing due emphasis on the local geological conditions.

5.2 Electrical Resistivity (ERT) and Induced Polarization (IPI) Tomography Sections

Given the tectonic setting of the study region, a high-resolution geological picture of the subsurface is needed to meet the basic objectives of the study. At shallower depth ranges combined ERT and IPI studies along eight profiles (Fig. 4) were implemented, which provided detailed subsurface geology up to 150 m depth. Usually, the presence of moist clay in the subsurface is an important factor facilitating landslides. Jongmans and Garambois (2007) remarked that very little attention is paid to IPI in landslide investigations even though it can distinguish moist clays from water wet sands. So, our choice of combined ERT and IPI studies in landslide investigations is unique in inferring the presence of clay in the subsurface, which also helped in the indirect mapping of subsurface faults.

In our study region, the subsurface lithology includes wet sand and schist in different stages of weathering. Figure 4 along with Table 1 provides all the relevant details of eight different ERT and IPI profiles. Tables 4 and 5 respectively outline the adopted resistivity–lithology and chargeability–lithology conversions. For the sake of brevity, we report here only the results along three profiles, AA', BB', and GG' (Fig. 4).

ERT, IPI, and shaliness percentage sections (Figs. 5, 6, 7) are correlated for the confirmation of various lithologies inferred from the resistivity sections. The IPI sections revealed the absence of clay horizons and the dominance of fresh schist/dry sand/wet sandy zones. The correlation between ERT, IPI, and relative shaliness percentage along three profiles are described below:

(a) Figure 5a depicts the ERT section along profile AA'. This profile was conducted across the limits of the landslide (Fig. 4) to ascertain the depth of the slip surface. A varied lithology is observed throughout the ERT section up to a depth of 90 m, and no continuous slip surfaces was noticed until that depth. The fresh schist (>8,000 Ωm) is observed at a shallow depth of 10–15 m range on the right side of the ERT section at surface distances of 420–520 m where, in the central part of the profile, hard rock (fresh schist) is observed at much greater depth (80 m). A zone of low resistivity of 500–1,000 Ωm (highly weathered schist) overlain by a high resistivity zone of 1,000–3,000 Ωm (semi-weathered schist) was found 10–15 m below the surface, in

Table 3 Resistivity–lithology conversion

| Resistivity in Ωm	Rock type
<40	Clay
40–150	Wet sandy clay
150–500	Wet sand
500–1,000	Highly weathered schist
1,000–3,000	Semi-weathered schist
3,000–5,000	Moderately weathered schist
5,000–8,000	Relatively fresh schist
>8,000	Fresh schist/dry sand

Table 4 Chargeability–lithology conversion

True chargeability in mV/V	Probable rock type
<30	Fresh schist/dry sand/wet sand
30–60	Highly weathered schist
60–130	Sandy clay
>130	Clay

Table 5 Summary of fault analysis of Salna village sinking zone

Profile	Faults	Throw (L–R)	Depth (m)	Profile	Faults	Throw (L–R)	Depth (m)
AA′	F1	D/U	1,361.75	GG′	F31	D/U	1,370.50
	F2	U/D	1,347.875		F32	U/D	1,346.125
	F3	U/D	1,359.125		F33	U/D	1,357.50
	F4	D/U	1,360.75		F34	D/U	1,342.25
BB′	F5	D/U	1,370.50	HH′	F35	D/U	1,383.50
	F6	D/U	1,365.625		F36	U/D	1,385.125
	F7	U/D	1,383.50		F37	D/U	1,383.75
	F8	D/U	1,377.00		F38	D/U	1,373.75
	F9	U/D	1,383.50		F39	U/D	1,373.75
	F10	D/U	1,367.25		F40	U/D	1,380.25
	F11	U/D	1,373.75		F41	D/U	1,373.75
	F12	U/D	1,374.125	II′	F42	D/U	1,310.325
CC′	F13	U/D	1,351.00		F43	D/U	1,381.875
	F14	D/U	1,360.75		F44	D/U	1,373.75
DD′	F15	D/U	1,368.875		F45	D/U	1,367.25
	F16	D/U	1,372.125		F46	U/D	1,378.625
	F17	U/D	1,375.375		F47	U/D	1,383.50
	F18	U/D	1,380.25	JJ′	F48	D/U	1,373.75
	F19	D/U	1,373.75		F49	D/U	1,359.125
	F20	U/D	1,385.00		F50	D/U	1,362.75
	F21	D/U	1,367.25		F51	D/U	1,370.50
EE′	F22	D/U	1,378.675		F52	U/D	1,386.75
	F23	D/U	1,375.375		F53	U/D	1,381.875
	F24	U/D	1,377.00		F54	U/D	1,370.50
	F25	U/D	1,372.125	KK′	F55	D/U	1,360.75
	F26	U/D	1,359.125		F56	U/D	1,370.50
	F27	D/U	1,359.125		F57	D/U	1,360.75
FF′	F28	U/D	1,373.75				
	F29	U/D	1,381.925				
	F30	D/U	1,368.875				

between electrode numbers 35 and 43. A heterogeneity in the resistivity values up to a great depth produced perplexity about the internal structure of the landslide.

The IPI section along profile AA′ (Fig. 5b) shows the dominance of very low chargeability (<30 mV/V) material, presumably fresh schist/dry sand/wet sand. A relative higher
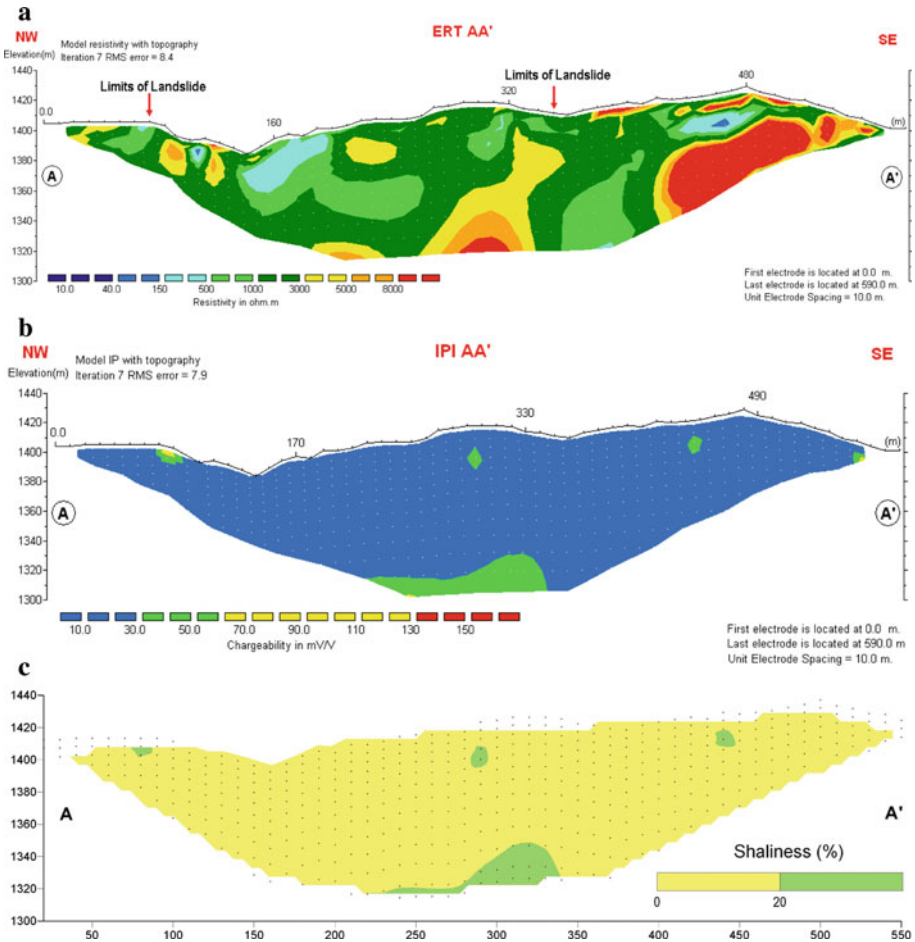
Fig. 5 Display of **a** resistivity, **b** chargeability and **c** relative shaliness percentage along profile AA' (Fig. 4)

chargeability zone is observed in between electrode numbers 23–35 at a depth of 80 m below the surface. The corresponding zone in the ERT section (Fig. 5a) shows a higher resistivity value. The high chargeability at such great depth may be due to the low resolving power of the IRIS equipment for IP data acquisition. As the relative shaliness percentage section (Fig. 5c) is derived from the true chargeability data, it provides similar information.

(b)   The ERT along BB' (Fig. 6a) was conducted in the central portion of the landslide parallel to the landslide axis (Fig. 4). The profile is of limited length due to the presence of buildings in Salna village and a busy road with heavy traffic. Except for the presence of two zones of high resistivity (>3,000 Ωm), most of the ERT exhibits intermediate resistivity zones representing wet sand (150–500 Ωm) and highly weathered schist (500–1,000 Ωm). In the IPI section along profile BB' (Fig. 6b), the dominance of very low chargeability (<30 mV/V) representing fresh schist/dry sand/ wet sand is observed, followed by a relatively higher chargeability of 30–60 mV/V
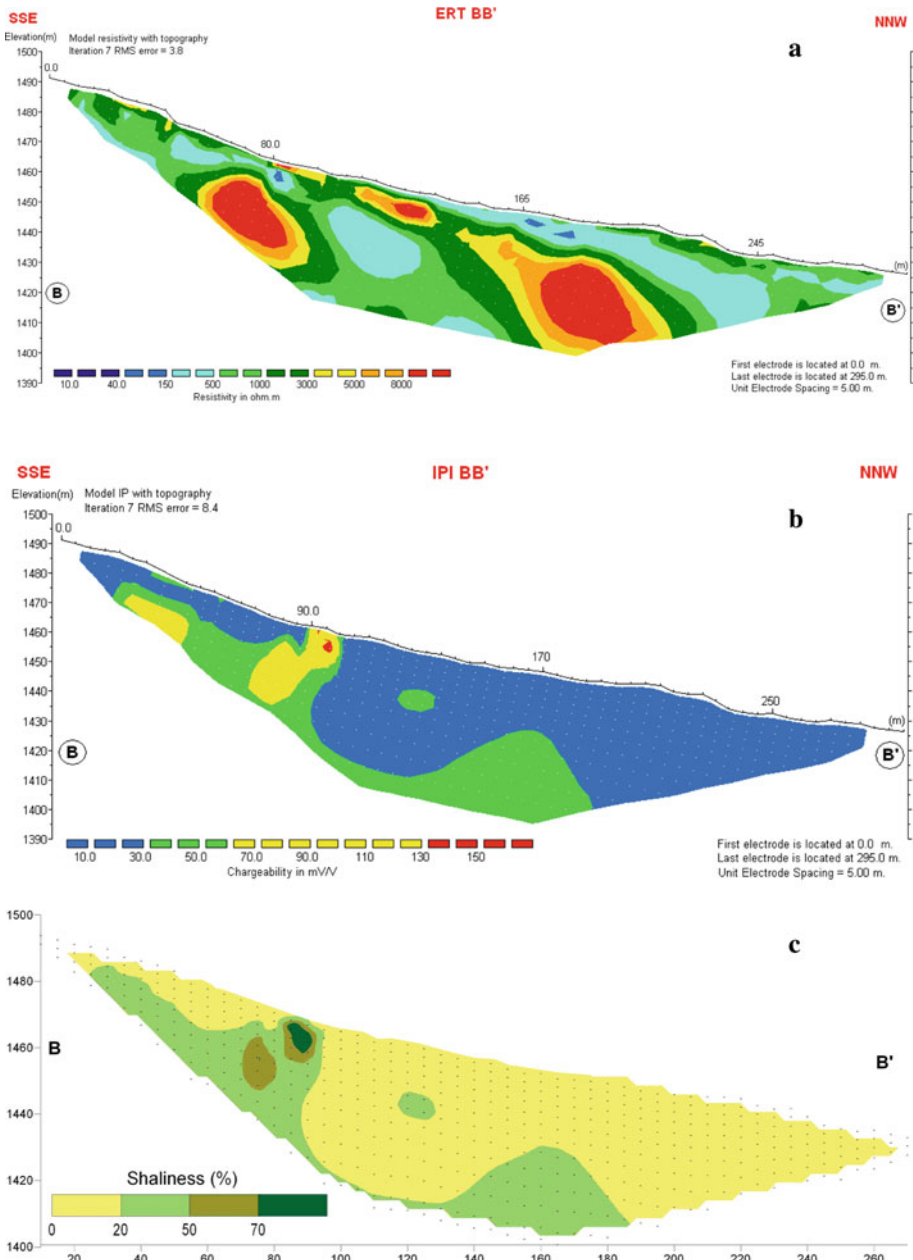
Fig. 6 Display of **a** resistivity, **b** chargeability and **c** relative shaliness percentage along profile BB′ (Fig. 4)

(highly weathered schist) and occasional patches of sandy clay material (70–130 mV/V). An increase in thickness of the low chargeability zone (<30 mV/V) is observed from crown to toe. This may be due to debris material deposited during the landslide process. The corresponding relative shaliness plot (Fig. 6c) also provides a similar result.
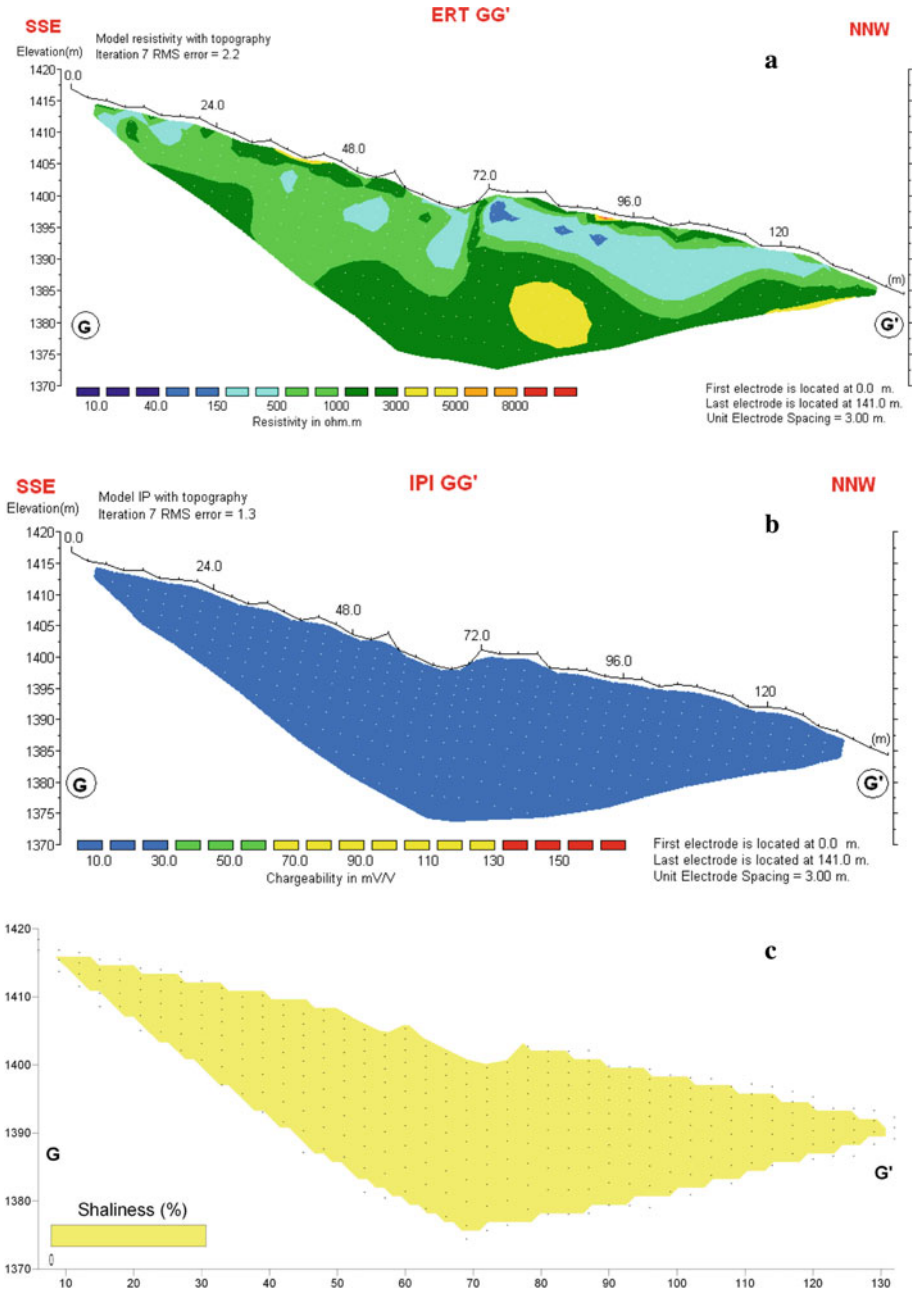
Fig. 7 Display of **a** resistivity, **b** chargeability and **c** relative shaliness percentage along profile GG′ (Fig. 4)

Relatively higher chargeability zones (30–60 mV/V) with respect to corresponding higher resistivity zones (Fig. 6a) may be due to low-resistive highly weathered schist zones surrounding the high resistivity fresh schist regions.

(c)   The ERT section along profile GG′ was conducted below the road in the toe region in continuation of ERT BB′ (Fig. 4). The length of the profile was limited to 144 m due to the steeply sloping ground. The first half of the tomogram lying in the lateral distance range of 0–72 m shows a dominance of highly weathered schist (500–1,000 Ωm), with occasional pockets of wet sandy (150–500 Ωm) material. Zones of highly resistive semi-weathered schist (1,000–3,000 Ωm) material are noticed in a depth range of 5–10 m. Similarly, the second half of the ERT (72–144 m.) shows the presence of wet sand (150–500 Ωm) up to a depth of 8 m along with few tiny pockets of wet sandy clay (40–150 Ωm). The high resistive zones (>1,000 Ωm) at the surface level are due to dislodged boulders. Thus, the ERT section along profile GG′ (Fig. 7a) shows a distribution of three major resistivity zones, namely wet sand (150–500 Ωm), highly weathered schist (500–1,000 Ωm), and semi-weathered schist (1,000–3,000 Ωm). The highly weathered schist is present mostly in the first half of the section between the surface distances 0–72 m. The IPI section (Fig. 7b) exhibits a very low chargeability (<30 mV/V) which may be due to low or nil clay content within the highly weathered schist material. The respective relative shaliness plot (Fig. 7c) explains the presence of sandy material in the subsurface as wet sand and semi-weathered schist will have very low chargeability values.

5.3 Gravity Data Analysis and Delineation of Fine Structure of Hard Rock

ERT sections along profiles AA′–HH′ revealed the presence of hard rock at a deeper level. So, the chosen common elevation datum was 1,385 m, and, accordingly, a common Bouguer datum for all the profiles was fixed. Station-wise surface elevations and relative Bouguer anomaly variation for profiles 1, 2, 3, 4, and 5 are shown in Fig. 8. The relative Bouguer anomaly contour map is depicted in Fig. 9. The qualitative interpretation of the Bouguer anomaly map has indicated the presence of several faults. Eleven profiles (AA′–KK′) were drawn across the strike of those inferred faults (Fig. 8). Those profiles yielded the fault parameters of 57 inferred faults (F1–F57), which are shown in Fig. 9. Table 5 summarizes all the details of the inferred faults (F1–F57).
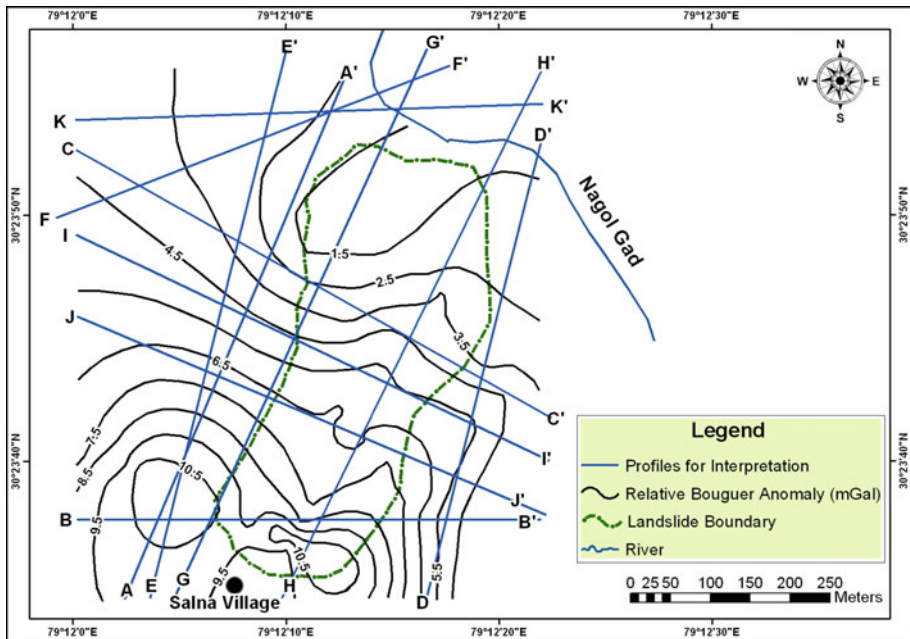
The gravity-inferred faults were extended laterally by considering their up-thrown and down-thrown signatures. In such a process, enough care is taken to weigh the strike of the fault and its depth of occurrence. As a result, Fig. 11 illustrates the location of gravity-inferred faults and their lateral extensions. Further, as per Fig. 9, the inferred faults are oriented mainly in two directions, namely the E-W trending faults, parallel to the regional Kande fault (Fig. 3) and NNE-SSW trending faults parallel to the Tangi anticline axis (Fig. 3). In addition, the faults parallel to the Kande fault have been dissected by later formed ones parallel to the Tangi anticline axis, thereby dividing the entire region into several blocks (Fig. 11).

The role of initial micro-gravity observations along five profiles (Fig. 4) ended up in generating the Bouguer anomaly map (Fig. 9) of the study region. Given the specific geological features of the study region, the choice of eleven gravity profiles (AA′–KK′) for the study region (Fig. 10) seemed to be a better strategy in deciphering the fine structure of the basement. At the outset, the number of inferred faults (57No.) seemed to be very much on the high side, but a close inspection of Figs. 10 and 11 reveals that they are indeed part of 13 curvilinear faults in total, with 8 of them parallel to the Tangi anticline and the other 5 parallel to the Kande fault. In our study region, micro-gravity played an important role in explaining the possible source(s) for the sinking and related landslides. As gravity anomaly
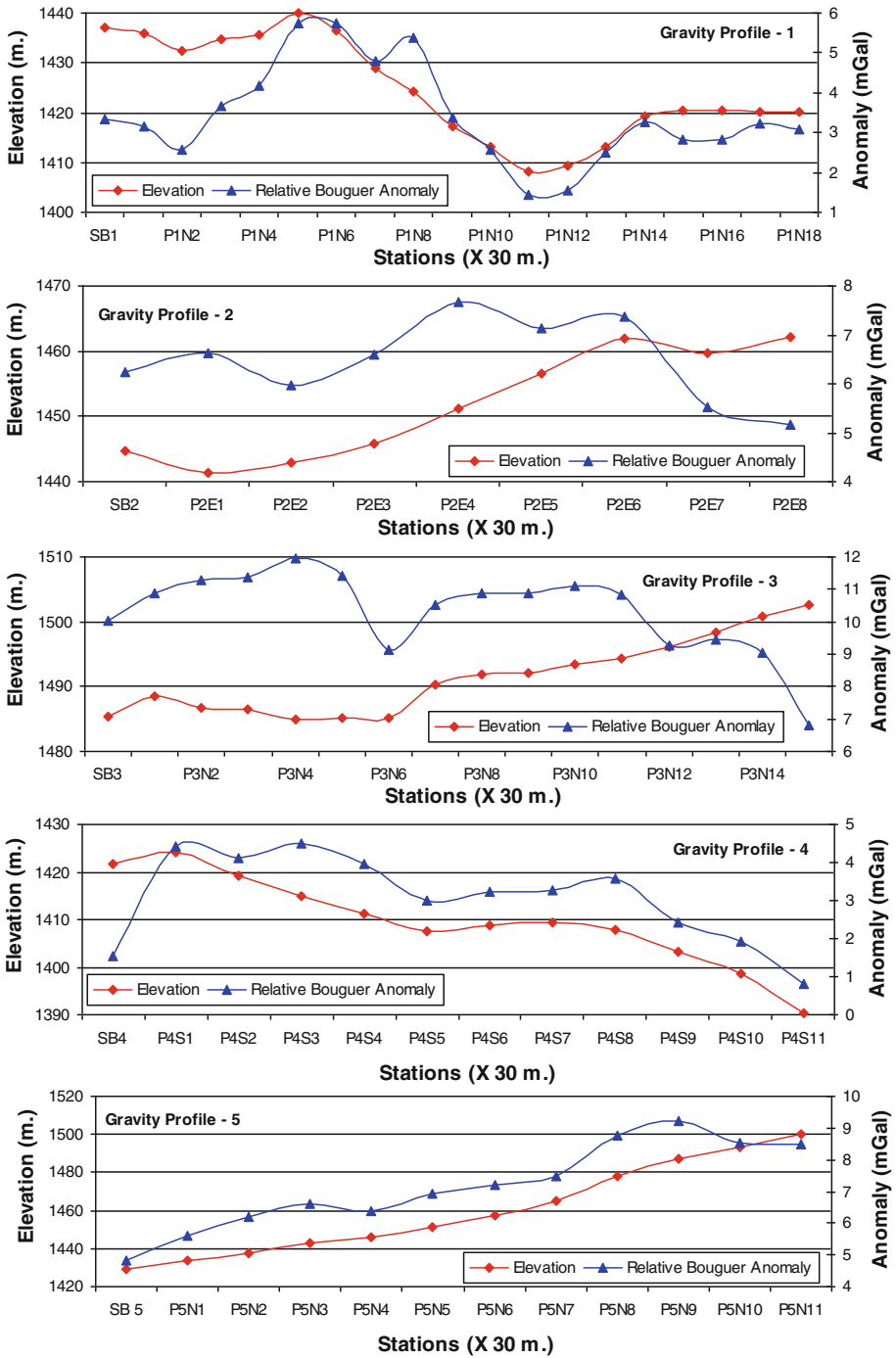
Fig. 8 Plots showing gravity station elevation versus relative Bouguer gravity anomaly along profiles 1 to 5 (Fig. 4)

Fig. 9 Bouguer anomaly contour map with eleven profiles (AA′ to KK′) for interpretation

sources are deep and extensive, it is natural to correlate the gravity-inferred faults with relevant signatures in the ERT and IPI sections.

5.4 Fault Signatures on ERT Sections and Their Correlation with Gravity-Inferred Faults

The positions of ERT profiles AA′–HH′ (Fig. 4) are overlaid on the map of gravity-inferred faults and their lateral extensions (Fig. 11) for checking possible fault signatures on the respective ERT sections. In such an effort, we have looked for independent analysis of ERT sections (Fig. 12) with gravity-inferred faults serving as the starting point. For that, the position of the gravity derived faults was projected onto the corresponding ERT sections, and the resulting fault signatures on ERT profiles AA′–HH′ are verified. For illustration purposes, we include here the ERT sections AA′ (Fig. 13) and GG′ (Fig. 14), respectively. Figures 13 and 14 reveal that gravity-inferred faults are almost vertical to subvertical in nature. We use the fault numbering adopted in Figs. 10 and 11. The resistivity values in all the ERT sections are expressed on a logarithmic scale.

(a) The ERT section along profile AA′ (Fig. 13) shows the presence of three faults, which coincide with the gravity-inferred faults, F14, F45, and F46 (Figs. 10, 11). Extension of the gravity-inferred fault F 14 is located in between electrode number 19 and 20. The left side of the fault is the down-thrown side and the right side is the up-thrown side. Similarly, the extended line of fault F 45 crosses the ERT section AA′ in between electrode number 32 and 33 at a depth of 1,365 m, and here, the left side of the fault is the up-thrown side and the right the down-thrown side. Fault F46 crosses the ERT in between electrode
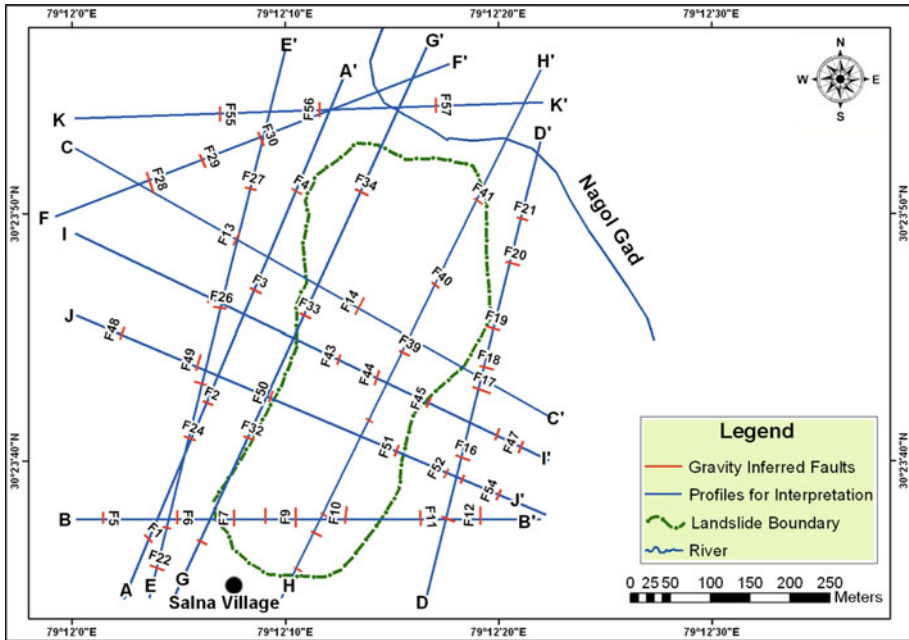
Fig. 10 Gravity inferred fault parameters are shown at respective locations on the profiles AA′–KK′ (Fig. 9). The depths and relative positions of up-thrown and down-thrown blocks of different inferred faults (F1–F57) are included in Table 5

43 and 44 at a depth of 1,371 m. The left side of the fault is up-thrown in relation to the right side.

(b) The gravity-inferred fault F19, which is located at depth of 1,374 m, just below the ERT section in between electrodes 22 and 23, has a clear signature on the ERT section GG′ (Fig. 14). The high resistive right block is not continuing on the left side of the inferred fault (Fig. 14). Further, the right block forms the up-thrown side of the fault F40. In view of the above, it is clear that gravity-inferred faults divide the hard rock at depth into a number of segments creating a blocky appearance. One can look for their signatures on the ERT sections. Accordingly, we have carried out an independent structural interpretation of the ERT/IPI section(s) using gravity analysis results in the background. At first sight, it seems that our interpretation approach is based heavily on gravity with ERT/IPI sections as support at shallow depth levels. However, we have shown that our analyses of both geophysical data sets are independent of each other. It is also true that not all gravity-inferred faults show up in the ERT sections. As the region happens to be a sinking zone, gravity played a key role in our investigations.

We presume that a relative movement of gravity-inferred blocks of hard rock, triggered by either neo-tectonic activity of region or monsoon rains, could serve as a source for landslides along with gradual sinking of the study region. Some of these faults could be traced in the ERT sections at shallow depth levels. Probably, the Chamoli earthquake in March 1999 could have triggered seismically induced ground movements in this region. The possible gravity-inferred faults that do not show up in ERT sections are like blind faults in the seismological literature and such sites could be the source(s) of future neo-tectonic activity including sinking and landslide triggering episodes.
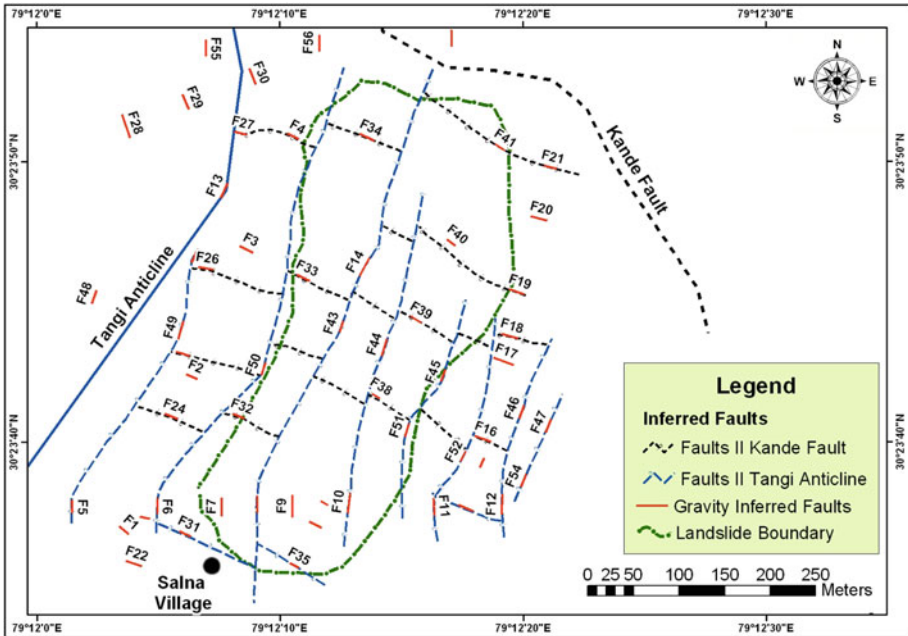
**Fig. 11** Illustration showing gravity inferred faults and their lateral extensions in the Salna village sinking zone. *Black* and *blue dashed lines* indicate faults parallel to the regional Kande Fault and the Tangi anticline axis, respectively
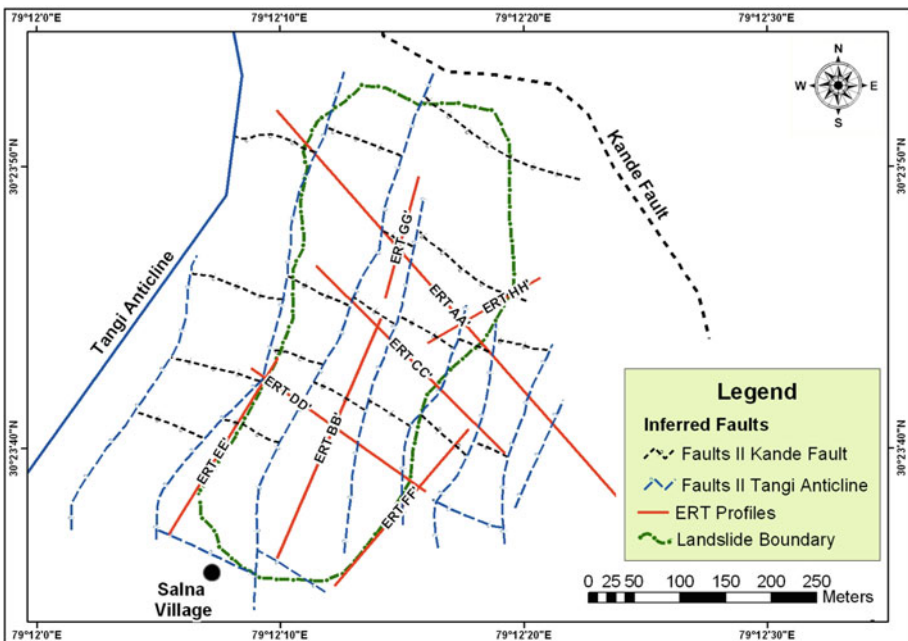
Fig. 12 A combined plot showing gravity inferred fault locations and ERT profiles
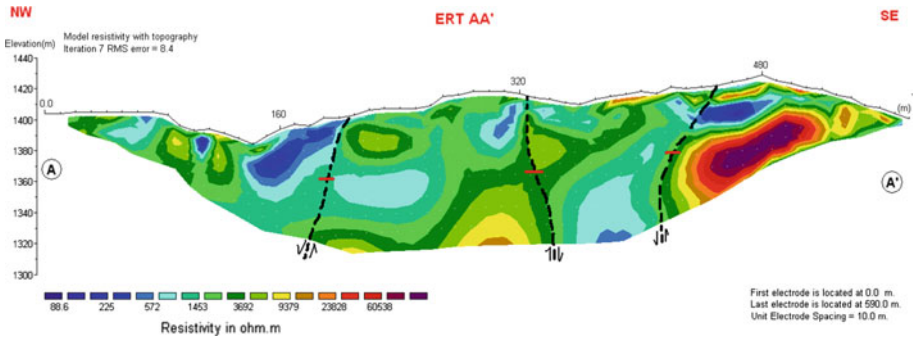
Fig. 13 ERT section along profile AA′ (Fig. 4). Resistivity values are expressed using a logarithmic scale. *Black dashed lines* are the inferred faults along with arrows showing up-thrown and down-thrown blocks. *Short horizontal segments in red color* refer to the depth of up-thrown blocks derived from gravity studies
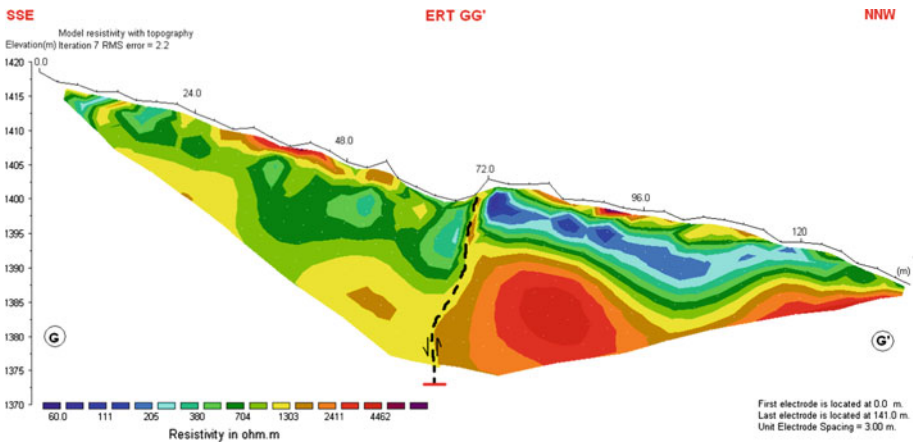
Fig. 14 ERT section along profile GG′ (Fig. 4). Resistivity values are expressed using a logarithmic scale. *Black dashed lines* are the inferred faults along with *arrows* showing up-thrown and down-thrown blocks. *Short horizontal segments in red* refer to the depth of up-thrown blocks derived from gravity studies

6 Geotechnical Investigations

Limited geotechnical investigations were carried out in the field and in the laboratory. The results of geotechnical investigations are mentioned below.

6.1 Classification of Landslide Material

Soil/debris samples were collected from different locations of the landslide region (Fig. 15). Laboratory analysis for grain size distribution and Atterberg limits were carried out, and the soil material was classified using the Indian Standard Soil Classification System (ISSCS). The grain size distribution plots of samples are depicted in Fig. 16. The classification of soil samples is given in Table 6.

6.2 Slope Stability Analysis

Detailed stability analyses were carried out for four representative slope cross sections (AA′–DD′ in Fig. 15) using the geological map and topographical data. The shear strength parameters (c and φ) were determined through direct shear tests of soil/debris samples and back analysis of critical slopes. The general slope condition is dry at the surface and moist at depth throughout the year. However, it becomes saturated during the monsoon. Considering the hydro-geological condition of the slope, the factor of safety (F) for all the sections was calculated both for dry and saturated conditions.

For illustration, we include a centrally located profile CC′ (Fig. 17), and the relevant stability analysis results in the form of output computer listing is included in section Appendix. The shear strength parameters c and φ for this slope profile are 2 and 16, respectively. The stability analysis is undertaken for rotational circular failure at depth. Table 7 outlines the minimum factor of safety for the slope cross sections (AA′–DD′) both for dry and for saturated conditions along with the coordinates of the critical slip surfaces.

6.2.1 Factor of Safety for Sections AA′–DD′

For profile AA′, the slide material is composed of an almost equal mixture of gravel, sand, and plastic fines and belongs to silty sand class (SM). The factor of safety (F) value varies from 1.013 in dry conditions to 0.0197 in saturation conditions, inferring thereby that this part of the slope is in the critical stage for both conditions. For profile BB′, the slide material is similar to that of section AA′. The factors of safety (F) are 1.153 and 1.078 for dry and saturation conditions, respectively. This shows that this part of slope may fail during the rainy season.
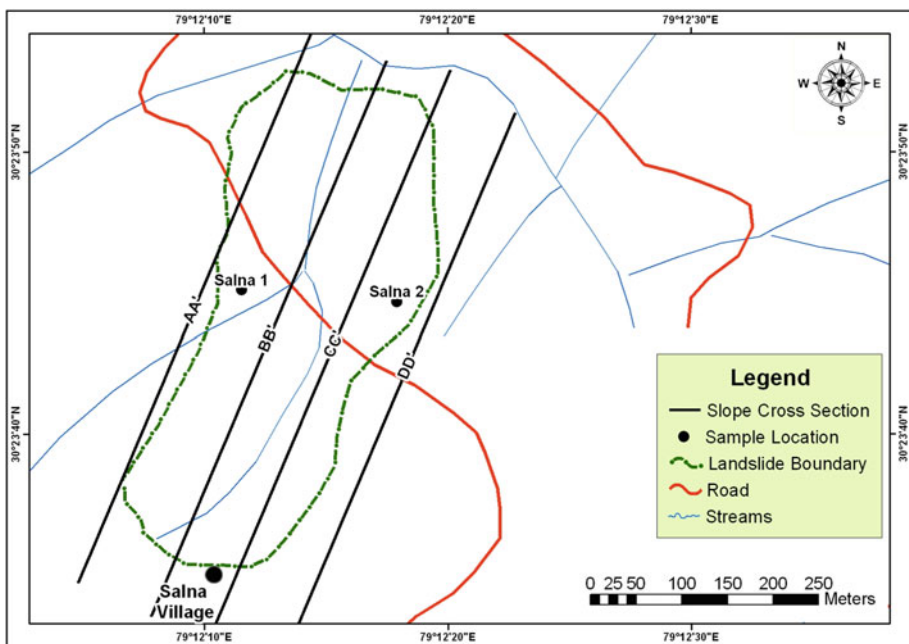
Fig. 15 Map showing the location of slope cross sections (AA′–DD′) and soil samples (Salna 1 and Salna 2). The landslide boundary is demarcated by the *green dashed line*

Grain Size Distribution (Salna - 1)

Grain Size Distribution (Salna - 2)
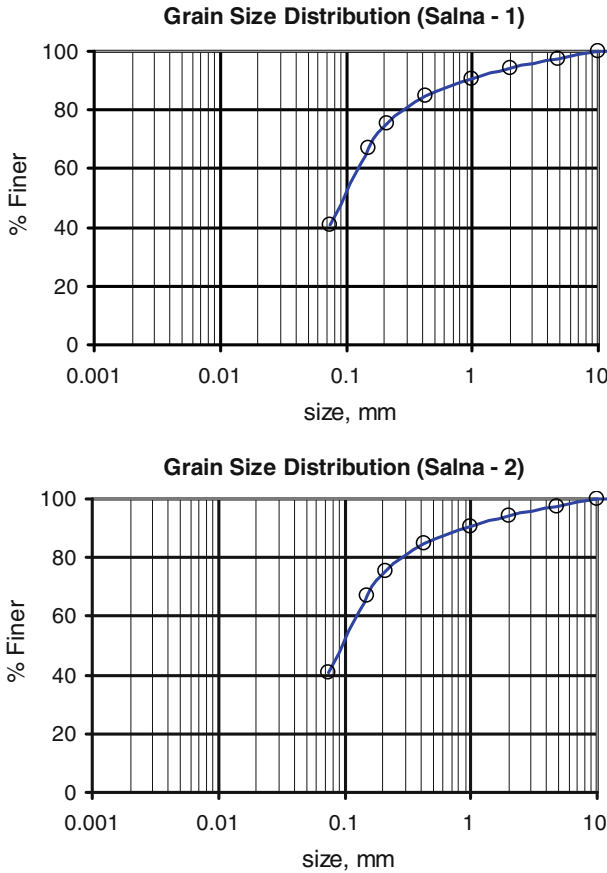
Fig. 16 Plot of grain size distributions for soil/debris samples of the Salna village sinking zone

Table 6 Classification of soil/debris sample

Sample no.	Grain size distribution			Plastic/ non-plastic	W_L	W_P	IP	Description	Class	Symbol
	Gravel %	Sand %	Fines %							
Salna-1	37.28	37.24	26.48	Plastic	41.05	41.0	0.5	Poorly graded sand silt mixture	Silty sand	SM
Salna-2	12.28	50.12	37.6	Non-plastic				Gravelly sand with non-plastic fines	Poorly graded sand	SP

W_L Liquid limit, W_P plastic limit, IP Plasticity Index

For profile CC′, the slide material is composed of sand with gravel and non-plastic fines and belongs to the poorly graded sand (SP) class. The factors of safety (F) are 1.197 and 1.176, respectively, thereby making the slope stable under both dry and wet conditions.
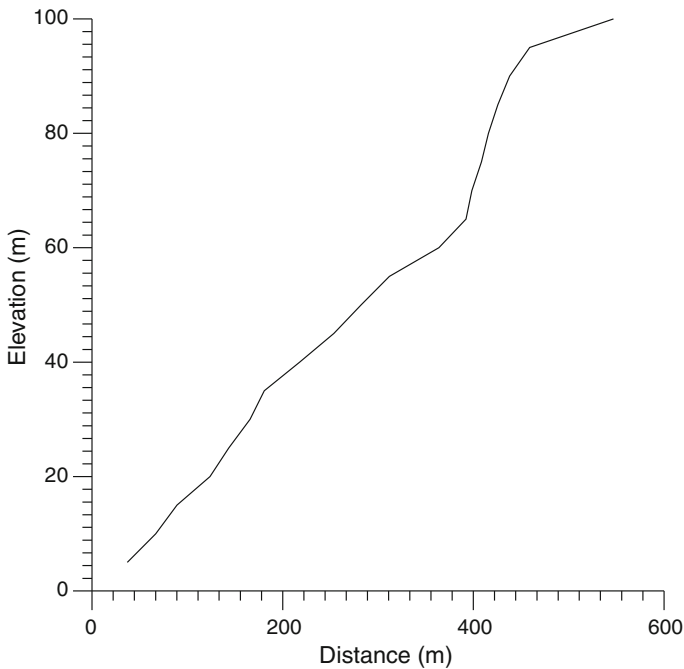
Fig. 17 Slope section CC′ (Fig. 15) for the geotechnical stability study

Table 7 Factor of safety of slope cross sections in dry and saturated condition along with values for cohesion and angle of internal friction

Slope cross section with	Factor of safety (F)	
	Dry condition (c, φ)	Saturated condition (c, φ)
AA′	1.0129 (2, 18)	0.9197 (2, 18)
BB′	1.1533 (2, 18)	1.0778 (2, 18)
CC′	1.1966 (2, 18)	1.1764 (2, 16)
DD′	1.1162 (2, 18)	1.0308 (2, 18)

c cohesion, φ angle of internal friction (in degrees)

For Profile DD′, the slide material is similar to that of section CC′. The factors of safety (F) are 1.116 and 1.031 for dry and saturated conditions, respectively. The slope along this section may fail during the rainy season.

7 Summary and Conclusions

(a) The Salna village sinking zone belongs to a completely different landslide mecha-nism, where the land subsidence is occurring along neo-tectonically activated faults, and this subsidence seems to be playing a crucial role in associated landslides peri-odically. For addressing the Salna sinking zone and associated landslide problem, we

have carried out integrated geophysical and geotechnical studies. The geophysical studies include ERT, IPI, and gravity methods. We have carried out eight ERT and IPI profiles and five gravity profiles spanning the study region. Additionally, we have collected soil samples at two locations and carried out relevant soil classification studies in a geotechnical laboratory. We have also carried out both in situ and geotechnical laboratory density measurements, which were used both in gravity data processing and slope stability studies.

(b) In view of the fact that gravity and tectonics go together, the more so for characterizing a sinking zone, our close micro-gravity data acquisition and its analysis have inferred a criss-cross network of faults in the subsurface. Unlike traditional landslide investigations, in our case study micro-gravity has played a key role in deciphering a fine subsurface structure at deeper depth level with respective fault signatures on ERT sections at shallow depths. Further, judging by the fault signatures on several ERT sections, it is inferred that these faults are vertical to subvertical in nature. The gravity-inferred faults seem to have divided the entire subsurface into several blocks, and the relative movement of these blocks is possibly leading to the sinking of the site.

(c) At first sight, the faults deciphered from gravity in Fig. 10 seem to be on the higher side in comparison to the limited number of micro-gravity measurements carried out along five profiles (Fig. 4). We feel that the role of gravity measurements must end with the preparation of a reliable Bouguer gravity map (Fig. 8) and its analysis needs to be tackled separately. Given the complex geological situation (Fig. 3) of the study region, we have considered 11 gravity profiles (Fig. 9) on our Bouguer anomaly map and carried out their analysis. This yielded 57 fault signatures along these profiles arising from a total of 13 faults, which run parallel to the major structural elements of the study region (Fig. 3).

(d) Although most of the surface geophysical methods are routinely being used for landslide investigations worldwide, our utilization of gravity along with ERT and IPI is novel. It has helped us to infer deep-seated subsurface fault networks. The absence of few gravity-inferred faults in shallow ERT sections may hint at blind faults, which could serve as future source(s) for geohazards in the study region. Thus, these integrated studies have yielded a better understanding of the mass-wasting mechanism for the study region.

(e) The slope stability investigation was conducted for the debris material at the site as per geotechnical norms. The results of slope stability analyses corroborate well with the geophysical inferences.

We have carried out geotechnical investigations along with field investigations as per the standard practice of geotechnical engineering. Soil sample sites and location of slope cross sections are indicated in Fig. 15. The grain size distribution plots are included in Fig. 16. Factors of safety are evaluated all along four sections (Fig. 15) and with critical values of cohesion and angle of internal friction, φ through standard back analysis. For illustration sake, we included slope stability analysis of profile CC′ (Fig. 17) and computation details in section Appendix.

Appendix

Stability analysis of Salna slope at section CC' (dry condition)

UNITS USED	->TONNE—METER—DEGREE
INPUT FILE NAME	->IAN.DAT
OUTPUT FILE NAME	->OAN.DAT

COORDINATES OF POINTS ALONG SLOPE->

$X(1) = .00000$	$Z(1) = .00000$
$X(2) = 37.13000$	$Z(2) = 5.00000$
$X(3) = 66.83000$	$Z(3) = 10.00000$
$X(4) = 89.10000$	$Z(4) = 15.00000$
$X(5) = 123.75000$	$Z(5) = 20.00000$
$X(6) = 143.55000$	$Z(6) = 25.00000$
$X(7) = 165.83000$	$Z(7) = 30.00000$
$X(8) = 180.68000$	$Z(8) = 35.00000$
$X(9) = 217.80000$	$Z(9) = 40.00000$
$X(10) = 253.69000$	$Z(10) = 45.00000$
$X(11) = 282.15000$	$Z(11) = 50.00000$
$X(12) = 311.85000$	$Z(12) = 55.00000$
$X(13) = 363.83000$	$Z(13) = 60.00000$
$X(14) = 392.29000$	$Z(14) = 65.00000$
$X(15) = 398.48000$	$Z(15) = 70.00000$
$X(16) = 408.38000$	$Z(16) = 75.00000$
$X(17) = 415.80000$	$Z(17) = 80.00000$
$X(18) = 425.70000$	$Z(18) = 85.00000$
$X(19) = 438.08000$	$Z(19) = 90.00000$
$X(20) = 459.11000$	$Z(20) = 95.00000$
$X(21) = 546.98000$	$Z(21) = 100.00000$

| $ROCK = -80.000$ | $RWL = .000$ | $XS = .000$ | $WI = .000$ |

continued

UNITS USED	->TONNE—METER—DEGREE
INPUT FILE NAME	->IAN.DAT
OUTPUT FILE NAME	->OAN.DAT

ZC = 1.000	ZWR = .500		
C = 2.000	PHI = 16.000	GAMA = 2.000	GAMAW = 1.000
BBAR = .000	AH = .100	AVR = .500	EQM = 7.000
ENTX = 89.100	ENTY = 15.000		
NEP = 0	NOPT = 1		
XEXITI = 143.550	XEXITL = 459.110		

CHECK F.S. FOR -AVR ALSO

F.S	DYN. DIS (M)	WEIGHT OF WEDGE (T)	AH CRITICAL	COORDINATES OF CENTER (XC, YC)	COORDINATES OF EXIT POINT	RADIUS R (M)
******						
1.9745	.000	.89E+03	.358	(112.20, 44.45)	(143.55, 25.00)	37.43
1.7629	.000	.22E+04	.312	(122.24, 44.28)	(163.55, 29.49)	44.22
1.3955	.000	20E+04	.224	(123.56, 86.87)	(183.55, 35.39)	79.71
1.3616	.000	.38E+04	.211	(136.02, 137.50)	(203.55, 38.08)	82.70
1.2879	.000	.37E+04	.189	(147.89, 131.98)	(223.55, 40.80)	131.18
1.3167	.000	.59E+04	.194	(155.79, 146.91)	(243.55, 43.59)	130.92
1.3195	.000	.75E+04	.193	(153.98, 215.81)	(263.55, 46.73)	147.82
1.2977	.000	.70E+04	.186	(184.94, 98.71)	(283.55, 50.24)	211.03
1.3647	.000	.16E+05	.197	(141.08, 146.95)	(303.55, 53.60)	127.25
1.3457	.000	.19E+05	.192	(194.18, 106.02)	(323.55, 56.13)	139.02
1.3440	.000	.22E+05	.190	(203.60, 113.04)	(343.55, 58.05)	150.74
1.3440	.000	.26E+05	.189	(213.02, 120.05)	(363.55, 59.97)	162.45
1.3410	.000	.29E+05	.187	(221.96, 127.85)	(383.55, 63.46)	174.32
1.2803	.000	.27E+05	.174	(220.41, 187.37)	(403.55, 72.56)	216.69
1.2497	.000	.30E+05	.167	(228.44, 186.27)	(423.55, 83.91)	220.80
1.1966	.000	.33E+05	.154	(235.41, 198.18)	(443.55, 91.30)	234.44
1.1966	.000	.33E+05	.154	(235.41, 198.18)	(443.55, 91.30)	234.44

Stability analysis of Salna slope at section CC' (saturated condition)

UNITS USED	->TONNE—METER—DEGREE
INPUT FILE NAME	->IAN.DAT
OUTPUT FILE NAME	->OAN.DAT

COORDINATES OF POINTS ALONG SLOPE->

X(1) = .00000	Z(1) = .00000
X(2) = 37.13000	Z(2) = 5.00000
X(3) = 66.83000	Z(3) = 10.00000
X(4) = 89.10000	Z(4) = 15.00000
X(5) = 123.75000	Z(5) = 20.00000
X(6) = 143.55000	Z(6) = 25.00000
X(7) = 165.83000	Z(7) = 30.00000
X(8) = 180.68000	Z(8) = 35.00000
X(9) = 217.80000	Z(9) = 40.00000
X(10) = 253.69000	Z(10) = 45.00000
X(11) = 282.15000	Z(11) = 50.00000
X(12) = 311.85000	Z(12) = 55.00000
X(13) = 363.83000	Z(13) = 60.00000
X(14) = 392.29000	Z(14) = 65.00000
X(15) = 398.48000	Z(15) = 70.00000
X(16) = 408.38000	Z(16) = 75.00000
X(17) = 415.80000	Z(17) = 80.00000
X(18) = 425.70000	Z(18) = 85.00000
X(19) = 438.08000	Z(19) = 90.00000
X(20) = 459.11000	Z(20) = 95.00000
X(21) = 546.98000	Z(21) = 100.00000
ROCK = -80.000	RWL = .000	XS = .000	WI = .000
ZC = 1.000	ZWR = 500		
C = 2.000	PHI = 16.000	GAMA = 2.000	GAMAW = 1.000

continued

UNITS USED	->TONNE—METER—DEGREE
INPUT FILE NAME	->IAN.DAT
OUTPUT FILE NAME	->OAN.DAT

BBAR = .100	AH = .100	AVR = .500	EQM = 7.000
ENTX = 89.100	ENTY = 15.000		
NEP = 0	NOPT = 1		
XEXITI = 143.550	XEXITL = 459.110	GAP = 20.000	

CHECK F.S. FOR -AVR ALSO

F.S *******	DYN. DIS (M)	WEIGHT OF WEDGE (T)	AH CRITICAL	COORDINATES OF CENTER (XC, YC)	COORDINATES OF EXIT POINT	RADIUS R (M)
1.8286	.000	.81E+03	.317	(11.72, 47.35)	(143.55, 25.00)	39.48
1.6177	.000	.22E+04	.269	(122.24, 44.28)	(163.55, 29.49)	44.22
1.2860	.000	.20E+04	.188	(124.04, 84.54)	(183.55, 35.39)	77.82
1.2447	.000	.38E+04	.174	(135.21, 83.65)	(203.55, 38.08)	82.70
1.1814	.000	.40E+04	.155	(137.86, 127.52)	(223.55, 40.80)	122.63
1.1886	.000	.49E+04	.155	(143.23, 158.09)	(243.55, 43.59)	152.99
1.2260	.000	.75E+04	.165	(155.79, 146.91)	(263.55, 46.73)	147.82
1.1843	.000	.71E+04	.153	(154.74, 211.50)	(283.55, 50.24)	207.18
1.1828	.000	.84E+04	.152	(160.47, 238.28)	(303.55, 53.60)	234.41
1.1764	.000	.98E+04	.150	(166.30, 268.91)	(323.55, 56.13)	265.38
1.2320	.000	.14E+05	.164	(181.89, 244.39)	(343.55, 58.05)	247.45
1.1948	.000	.13E+05	.153	(180.93, 320.29)	(363.55, 59.97)	318.80
1.2483	.000	.23E+05	.166	(212.30, 187.75)	(383.55, 63.46)	212.18
1.3057	.000	.32E+05	.178	(229.21, 138.45)	(403.55, 72.56)	186.74
1.2642	.000	.35E+05	.169	(235.77, 150.18)	(423.55, 83.91)	199.47
1.2284	.000	.39E+05	.161	(243.53, 159.93)	(443.55, 91.30)	211.79
1.2284	.000	.39E+05	.161	(243.53, 159.93)	(443.55, 91.30)	211.79

References

Bichler A, Bobrowsky P, Best M, Douma M, Hunter J, Calvert T, Burns R (2004) Three dimensional mapping of a landslide using a multi-geophysical approach: the Quesnel Forks landslide. Landslides 1:29–40

Bilham R, Gaur VK, Molnar P (2001) Himalayan seismic hazard. Science 293:1442–1444

Bláha P, Mrlina J, Nešvara J (1998) Gravimetric investigation of slope deformations. Explor Geophys Remote Sens Environ J 1:21–24

Bogoslovsky VA, Ogilvy AA (1977) Geophysical methods for investigation of landslides. Geophysics 42(3):562–571

Chambers JE, Wilkinson PB, Kuras O, Ford JR, Gunn DA, Meldrum PI, Pennington CVL, Weller AL, Hobbs PRN, Ogilvy RD (2011) Three-dimensional geophysical anatomy of an active landslide in Lias Group mudrocks, Cleveland Basin, UK. Geomorphology 125:472–484

Colangelo G, Lapenna V, Perrone A, Piscitelli S, Telesca L (2006) 2D Self-Potential tomographies for studying groundwater flows in the Varoc d'Izzo landslide (Basilicata, southern Italy). Eng Geol 88:274–286

Cosenza P, Marmet E, Rejiba F, Cui JY, Tabbagh A, Charlery Y (2006) Correlation between geotechnical and electrical data: a case study at Garchy in France. J Appl Geophys 60:165–178

Del Gaudio V, Wasowski J, Pierri P, Mascia U, Calcagnile G (2000) Gravimetric study of a retrogressive landslide in southern Italy. Surv Geophys 21:391–406

Drahor MG, Göktürkler G, Berge MA, Kurtulmus TÖ (2006) Application of electrical resistivity tomography technique for investigation of landslides: a case study from Turkey. Environ Geol 50:147–155

Erginal AE, Ozturk B, Ekinci YL, Demirci A (2009) Investigation of the nature of slip surface using geochemical analyses and 2-D geoelectrical tomography: a case study from Lapseki area, NW Turkey. Environ Geol 58(6):1164–1175

Friedel S, Thielen A, Springman SM (2006) Investigation of a slope endangered by rainfall induced landslides using 3D resistivity tomography and geotechnical testing. J Appl Geol 60:100–114

Gaur VK, Chander R, Sarkar I, Khattri KN, Sinvhal H (1984) Seismicity and the state of stress from investigations of local earthquakes in the Kumaon Himalaya. Tectonophysics 118:243–251

Havenith HB, Jongmans D, Abdrakhmatov K, Trefois P, Delvaux D, Torgoev IA (2000) Geophysical investigations of seismically induced surface effects: case study of a landslide in the Suusamyr valley, Kyrgyzstan. Surveys Geophys 21:349–369

Hayley K, Bentley LR, Gharibi M, Nightingále M (2007) Low temperature dependence of electrical resistivity: implications for near surface geophysical monitoring. Geophys Res Lett 34:L18402

Israil M, Pachauri AK (2003) Geophysical characterization of a landslide site in the Himalayan foothill region. J Asian Earth Sci 22:253–263

Jin G, Torres-Verdin V, Devarajan S, Toumelin E, Thomas EC (2007) Pore scale analysis of the Waxman-Smits shaly sand conductivity model. Petrophysics 48(2):104–120

Jomard H, Lebourg T, Eric T (2007) Identification of the gravitational boundary in weathered gneiss by geophysical survey: La Clapière landslide (France). J Appl Geophys 62:47–57

Jongmans D, Garambois S (2007) Geophysical investigation of landslides: a review. Bull De la Societe Geologique De France 178(2):101–112

Kayal JR (2001) Microearthquake activity in some parts of the Himalaya and the tectonic model. Tectonophysics 339:331–351

Khattri KN, Tyagi AK (1983) Seismicity patterns in the Himalayan plate boundary and identification of the areas of high seismic potential. Tectonophysics 96:281–297

Khattri KN, Chander R, Gaur VK, Sarkar I, Kumar S (1989) New seismological results on the tectonics of the Garhwal Himalaya. Proc Indian Acad Sci 98:91–109

Kumar G, Agarwal NC (1975) Geology of Srinagar-Nandprayag Area (Alkananda Valley), Chamoli, Garhwal and Tehri Garhwal Districts, Kumaun Himalaya, Uttar Pradesh. Himal Geol 5:29–59

Lapenna V, Lorenzo P, Perrone A, Piscitelli S, Sdao F, Rizzo E (2003) High resolution geoelectrical tomographies in the study of Giarrossa landslide (southern Italy). Bull Eng Geol Environ 62:259–268

Lapenna V, Lorenzo P, Perrone A, Piscitelli S, Rizzo E, Sdao F (2005) 2D electrical resistivity imaging of some complex landslides in the Lucanian Apennine chain, southern Italy. Geophysics 70(3):B11–B18

Lebourg T, Tric E, Guglielmi Y, Cappa F, Charmoille A, Bouissou S (2003) Geophysical survey to understand failure mechanisms involved on deep sated landslides. Geophys Res Abstr 5:01043

Lebourg T, Binet S, Tric E, Jomard H, El Bedoui S (2005) Geophysical survey to estimate the3D sliding surface and the 4D evolution of the water pressure on part of a deep seated landslide. Terra Nova 17(5):399–406

Loj M (2010) Expected discontinuous terrain deformation with the micro-gravity method in a selected area of coal exploration. In: Near surface 2010—16th European meeting of environmental and engineering geophysics, 6–8 Sept 2010, Zurich, Switzerland

Loke MH (2006) RES2DINV ver 3.55 Rapid 2D resistivity and IP inversion using the Least-squares method, Software Manual, p 139

Loke MH, Barker RD (1995a) Least-squares deconvolution of apparent resistivity pseudosections. Geophysics 60:1682–1690

Loke MH, Barker RD (1995b) Improvements to the Zohdy method for the inversion of resistivity sounding and pseudosection data. Comput Geosci 21:321–332

Loke MH, Barker RD (1996a) Rapid Least-squares inversion of apparent resistivity pseudo-sections using a quasi-Newton method. Geophys Prospect 44:131–152

Loke MH, Barker RD (1996b) Practical techniques for 3D resistivity surveys and data inversion. Geophys Prospect 44:499–523

Mauritsch HJ, Seiberl W, Ranier A, Romer A, Schneiderbauer K, Sendlhoper GP (2000) Geophysical investigation of large landslides in the Carnic region of southern Austria. Eng Geol 56:373–388

McCann DM, Forster A (1990) Reconnaissance geophysical methods in landslide investigations. Eng Geol 29:59–78

Mondal SK, Sastry RG, Gautam PK, Pachauri AK (2007) High resolution resistivity imaging of Naitwar Bazar Landslide, Garhwal Himalaya, India. In: Proceedings of 20th symposium on the application of geophysics to engineering and environmental problems (SAGEEP), pp 629–635

Mondal SK, Sastry RG, Gautam PK, Pachauri AK (2008) High resolution 2D electrical resistivity tomography to characterize active Naitwar Bazar Landslide, Garhwal Himalaya, India—a case study. Curr Sci 94(7):871–875

Ni JF, Barazangi M (1984) Seismotectonics of the Himalayan collision zone: geometry of the underthrusting Indian plate beneath the Himalaya. J Geophys Res 89:1147–1163

Niwas S, Gupta PK, de Lima OAL (2007) Nonlinear electrical conductivity response of shaly-sand reservoir. Curr Sci 92(5):612–617

Oldenburg DW, Li Y (1994) Inversion of induced polarization data. Geophysics 59:1327–1341

Pachauri AK, Pant M (1992) Landslide hazard mapping based on geological attributes. Eng Geol 32(1–2):81–100

Park S (1998) Fluid migration in the vadose zone from 3D inversion of resistivity monitoring data. Geophysics 63:41–51

Perrone A, Iannuzzi A, Lapenna V, Lorenzo P, Piscitelli S, Rizzo E, Sdao F (2004) High-resolution electrical imaging of the Varco d'Izzo earthflow (southern Italy). J Appl Geophys 56:17–29

Piegari E, Catandella V, Di Mario L, Milano L, Nicodemi M, Solovieri MG (2009) Electrical resistivity tomography and statistical analyses in landslide monitoring: a conceptual approach. J Appl Geophys 68(2):151–158

Ranjan G, Rao ASR (2005) Basic and applied soil mechanics. New Age International (P) Limited, Publishers, New Delhi

Rao NP, Kumar P, Kalpna T, Tsukuda T, Ramesh DS (2006) The devastating Muzaffarabad earthquake of 8 October 2005: new insights into Himalayan seismicity and tectonics. Gondwana Res 9:365–378

Rautela P, Lakhera RC (2000) Landslide risk analysis between Giri and Tons Rivers in Himachal Himalaya (India). JAG 2(3/4):153–160

Ravindran KV, Philip G (1999) 29 March 1999 Chamoli earthquake: a preliminary report on earthquake-induced landslides using IRS-1C/1D data. Curr Sci 77(1):21–25

Revil A, Cathles LM, Losh S Nunn JA (1998) Electrical conductivity in shaly sands with geophysical applications. J Geophys Res 103(B10):23925–23936

Revil A, Hermitte D, Spangenberg E Cochémé JJ (2002) Electrical properties of zeolitized volcanoclastic materials. J Geophys Res 107(B8):2155–2168

Rybakov V, Goldshmidt V, Fleischer L, Rolstein Y (2001) Cave detection and 4-D monitoring: a micro-gravity case history near the Dead Sea. Lead Edge 8:896–900

Saha AK, Gupta RP, Sarkar I, Arora MK, Csaplovics E (2005) An approach for GIS-based statistical landslide susceptibility zonation—with a case study in the Himalayas. Landslides 2(1):61–69

Saraf AK (2000) IRS-1C-PAN depicts Chamoli earthquake induced landslides in Garhwal Himalayas, India. Int Remote Sens 21(12):2345–2352

Sarkar S, Kanungo DP (2002) Landslides in relation to terrain parameters—a remote sensing and GIS approach. Map India—2002

Sarkar I, Chander R, Khattri KN, Sharma PK (1993) Evidence from small magnitude earthquakes on the active tectonics of Northwest Garhwal Himalaya. J Himal Geol 4:279–284

Sastry RG, Mondal SK, Pachauri AK (2006) 2D Electrical resistivity tomography of a landslide in Garhwal Himalaya. In: Proceedings of 6th international conference & exposition on petroleum geophysics (Kolkata). Society of Petroleum Geophysicists, India, pp 997–1001

Sastry RG, Mondal SK, Gautam PK, Pachauri AK (2007) Integrated geophysical approach for mapping an active landslide in Himalaya. In: Proceedings of 20th symposium on the application of geophysics to engineering and environmental problems (SAGEEP), pp 248–254

Sastry RG, Mondal SK, Gautam PK, Pachauri AK (2008) Electrical resistivity tomography and gravity studies for active landslide characterization at Naitwar, Garhwal Himalaya, India. In: Poster presentation in 7th international conference & exposition on petroleum geophysics, Hyderabad, organized by Society of Petroleum Geophysicists, India

Schmutz M, Guerin R, Andrieux P, Maquaire O (2009) Determination of the 3-D structure of an earthflow by geophysical methods the case of Super Sauze, in the French southern Alps. J Appl Geophys 68(4):500–507

Serra O (1984) Fundamentals of welllog interpretation vol 1: the acquisition of logging data. Elsevier, Amsterdam

Shevnin V, Mousatov A, Ryjov A, Delgado-Rodriquez O (2007) Estimation of clay content in soil based on resistivity modeling and laboratory measurements. Geophys Prospect 55(2):265–275

Telford WM, Geldart LP, Sheriff RE (1990) Applied geophysics. Cambridge University Press, London

Wilkinson PB, Chambers JE, Meldrum PI, Gunn DA, Ogilvy RD, Kuras O (2010) Predicting the movements of permanently installed electrodes on an active landslide using time-lapse geoelectrical resistivity data only. Geophys J Int 183:543–556

Yang C, Liu H, Lee C (2004) Landslide investigation in the Li-Shan area using resistivity image profiling method. In: Paper presented in SEG 74th annual meeting, pp 1417–1420

Zanetell (2011) IP and seismic 3D imaging of landslides, Publ. No. FHWA-CFC/TD-11-006, US Department Of Transportation, Federal Highway Adminstration, pp 1–128